ChemPubSoc Europe

DOI: 10.1002/cphc.201801088

CHEMPHYSCHEM Articles

Special Issue

Pd^{2+}-Initiated Formic Acid Decomposition: Plausible Pathways for C-H Activation of Formate

Won Jong Lee[+],[a] Yeon Jin Hwang[+],[a, b] Joohoon Kim,[b, c] Hyangsoo Jeong,*[a] and Chang Won Yoon*[a, b, d]

Formic acid (HCOOH, FA) has long been considered as a promising hydrogen-storage material due to its efficient hydrogen release under mild conditions. In this work, FA decomposes to generate CO_2 and H_2 selectively in the presence of aqueous Pd^{2+} complex solutions at 333 K. $Pd(NO_3)_2$ was the most effective in generating H_2 among various Pd^{2+} complexes explored. Pd^{2+} complexes were *in situ* reduced to Pd^0 species by the mixture of FA and sodium formate (SF) during the course of the reaction. Since C–H activation reaction of Pd^{2+}-bound formate is occurred for both Pd^{2+} reduction and H_2/CO_2 gas generation, FA decomposition pathways using several Pd^{2+} species were explored using density functional theory (DFT) calculations. Rotation of formate bound to Pd^{2+}, β-hydride elimination, and subsequent CO_2 and H_2 elimination by formic acid were examined, providing different energies for rate determining step depending on the ligand electronics and geometries coordinated to the Pd^{2+} complexes. Finally, Pd^{2+} reduction toward Pd^0 pathways were explored computationally either by generated H_2 or reductive elimination of CO_2 and H_2 gas.

1. Introduction

To address the increasing energy and environmental issues due to the ever-increasing use of fossil fuels, substantial efforts are being made to employ renewable energy resources for the future.[1] However, due to the intermittent and unpredictable nature of renewable energy production, an efficient energy carrier capable of storing and transporting the produced renewable energy on demand is needed. In this regard, hydrogen has long been recognized as a clean and sustainable energy carrier that meets the global energy demand because of its substantially high gravimetric energy density of 142 MJ kg^{-1}, much higher than those of gasoline and natural gas.[2] In addition, use of hydrogen in conjunction with fuel cells can maximize the efficiencies of relevant energy systems while releasing only water, which is environment-friendly. However, the low volumetric energy density of hydrogen (10.7 kJ L^{-1})[3] limits its use in different stationary fuel cell applications such as hydrogen refueling stations, off-grid power generators, and distributed power generation systems. Thus, a safe and reliable method must be developed, which can store mass quantities of hydrogen in a unit volume for utilizing renewable energy in an efficient manner.

In this context, numerous liquid chemicals possessing high volumetric hydrogen storage densities of >50 g-H_2/L have been studied extensively. These liquid chemicals could also be economically viable for transport using the currently existing infrastructure. One such potentially promising liquid chemical is formic acid (FA, HCOOH) which has a high volumetric hydrogen storage capacity of 53 g-H_2/L. Furthermore, the hydrogen atoms stored chemically in FA can be released rapidly as molecular hydrogen at temperatures of <70 °C, in the presence of an appropriate catalyst (Eq. 1, dehydrogenation pathway).[4] In addition to the H_2-release pathway, another thermodynamically favorable dehydration reaction is also possible during FA decomposition (Eq. 2, dehydration pathway), producing carbon monoxide that is detrimental to polymer electrolyte membrane fuel cell (PEMFC) applications.[5] Hence, for FA to be highly useful, the undesired dehydration reaction needs to be suppressed.

$$HCOOH\ (l) -> CO_2\ (g) + H_2\ (g)\ (\Delta G^\circ = -32.9\,kJ\,mol^{-1}) \quad (1)$$

$$HCOOH\ (l) -> CO\ (g) + H_2O\ (l)\ (\Delta G^\circ = -12.4\,kJ\,mol^{-1}) \quad (2)$$

In previous studies, significant attention has been focused on developing highly selective and active homogeneous and

[a] Dr. W. J. Lee,[+] Y. J. Hwang,[+] Dr. H. Jeong, Prof. Dr. C. W. Yoon
Center for Hydrogen·Fuel Cell Research, Korea Institute of Science and Technology (KIST), 5 Hwarang-ro 14-gil, Seongbuk-gu, Seoul 02792, Republic of Korea
E-mail: cwyoon@kist.re.kr
hsjeong@kist.re.kr

[b] Y. J. Hwang,[+] Prof. Dr. J. Kim, Prof. Dr. C. W. Yoon
KHU-KIST Department of Converging Science and Technology, Kyung Hee University, 26 Kyungheedae-ro, Dongdaemun-gu, Seoul 02447, Republic of Korea

[c] Prof. Dr. J. Kim
Department of Chemistry, Research Institute for Basic Sciences, Kyung Hee University, 26 Kyungheedae-ro, Dongdaemun-gu, Seoul, 02447, Republic of Korea

[d] Prof. Dr. C. W. Yoon
Division of Energy and Environment Technology, KIST School, Korea University of Science and Technology (UST), 5 Hwarang-ro 14-gil, Seongbuk-gu, Seoul 02792, Republic of Korea

[+] These authors contributed equally.

Supporting information for this article is available on the WWW under https://doi.org/10.1002/cphc.201801088

An invited contribution to a Special Issue on Hydrogen Energy

heterogeneous catalysts for FA dehydrogenation pathway. For homogeneous catalysis, iron, rhodium, ruthenium, and iridium-based catalysts have been reported. For example, Laurenczy et al. reported the decomposition of FA using $RuCl_3 \cdot xH_2O$ and water-soluble meta-trisulfonated triphenylphosphine (TPPTS) ligand.[6] Mechanistic studies indicated that formate anion binds to the metal center and undergoes subsequent β-elimination to yield ruthenium hydride species coordinated to CO_2 ligand. Subsequently, either the dissociation of CO_2 and H_2 by formic acid continues the catalytic cycle or the formate could bind to ruthenium hydride species and CO_2 and H_2 might be released via ruthenium dihydride intermediate.[7] Highly active iridium(III) bipyridine-based catalyst was developed by Himeda[8] while rhodium(III) bipyridine-based catalyst was reported by Fukuzumi et al. as active catalysts in FA dehydrogenation.[9] Moreover, a non-noble metal catalyst such as an iron complex was also shown to be highly active for FA dehydrogenation, as reported by Beller[10] and Hazari et al.[11]

In contrast, heterogeneous catalytic systems are mostly composed of Pd^0 or Au^0 nanoparticles on solid supports. Though these catalysts were developed by modification of support materials or active sites by the addition of secondary metals such as Ag^0 or Au^0, Pd^0 remains the highly active metal in FA dehydrogenation.[12–15] Recently, in monometallic Pd-based catalysts, active catalytic systems containing both Pd^0 and Pd^{2+} oxidation states have been reported, and reduction of Pd^{2+} has been proposed to be the reason for its decreased reactivity in FA dehydrogenation.[16] In 2016, single-site Pd^{2+} on N-doped carbon was reported to be the active site in FA dehydrogenation by near-edge X-ray absorption fine structure (NEXAFS) and X-ray photoelectron spectroscopy (XPS) studies.[17] DFT studies indicated that dehydrogenation proceeded through C–H activation to afford palladium hydride and a carboxyl fragment rather than O–H activation leading to formate binding pathway. However, there have not been many mechanistic studies reported in understanding the role of Pd^{2+} as an active site.

In this paper, we report our preliminary study of decomposition of FA using Pd^{2+} complexes in aqueous solution. Though the reduction of Pd^{2+} to form metallic Pd was observed under the reaction condition, the dissociation of C–H bond of FA by Pd^{2+} should be occurred. Computational pathways of the FA dehydrogenation using isolated Pd^{2+} species are explored. Mechanistic pathways through the coordination of formate, β-hydride elimination, and subsequent dissociation of CO_2 and H_2 by formic acid are calculated by density functional theory (DFT) studies. Finally, ligand modifications varying electronics were examined to explore energy barriers in the dehydrogenation reaction.

2. Results and Discussion

2.1. Formic Acid Decomposition over Pd(II) Complexes

A number of Pd^{2+} complexes were initially employed to accelerate FA decomposition in the presence of formate as an additive at 60 °C. As depicted in Figure 1, the rates of H_2-release were highly dependent upon the kind of Pd^{2+} compound. For instance, Pd^{2+} complexes with chloride ligands such as $PdCl_2$, Na_2PdCl_4, and $Pd(NH_3)_4Cl_2$ showed nearly no activity in FA decomposition for over 1 h, with less than 50 mL of gases being produced. In contrast, the dehydrogenation kinetics improved significantly upon utilization of $Pd(NO_3)_2$ and $Pd(OAc)_2$, suggesting the importance of coordinating ligands. In particular, $Pd(NO_3)_2$ exhibited the highest activity among the complexes employed, releasing ~330 mL of gases over 3 h. It was notable that the initial orange color of the aqueous solution containing Pd^{2+} complex turned black, along with the formation of black particles, as the reaction proceeded. The results indicated that the reduction of Pd^{2+} ion occurred under the reaction conditions in the presence of the mixture of formic acid and sodium formate.

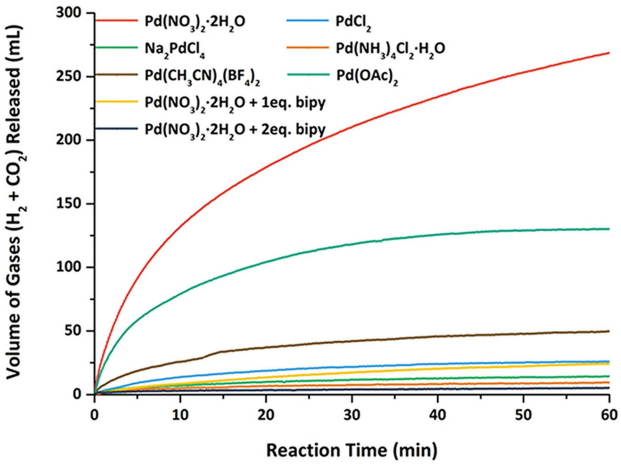

Figure 1. Volume of the gases released ($H_2 + CO_2$) as a function of time for formic acid (FA) decomposition over different Pd^{2+} complexes.

UV-Vis spectroscopy was employed to monitor the rate of Pd^{2+} reduction *in situ*. Figure 2 presents a fast decrease in

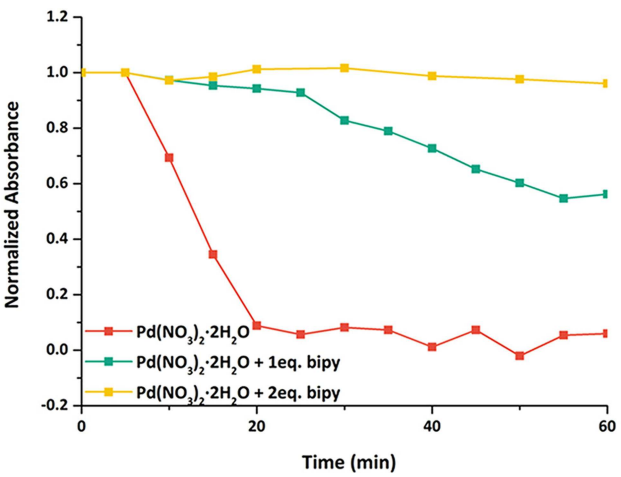

Figure 2. Changes in absorbance of Pd^{2+} species as a function of time.

absorbance at $\lambda = 345$ nm attributed to Pd^{2+} at $Pd(NO_3)_2$, again indicating the reduction of Pd^{2+} species. For Pd^{2+} to be reduced, the formate reactant needed to be coordinated to it by ligand exchange reactions. If a ligand is coordinated strongly at the Pd^{2+} center, the ligand exchange reaction with formate would be slow, resulting in retardation of the reduction process. In this context, an additional ligand, 2,2′-bipyridine (bipy) was employed to induce strong interaction between Pd^{2+} and bipy. When a sonicated aqueous solution of 2,2′-bipy and $Pd(NO_3)_2$ in the molar ratio of 1:1 was tested, the solution showed slow decrease in absorbance at $\lambda = 345$ nm, indicating sluggish Pd^{2+} reduction (Figure 2). Furthermore, the aqueous solution containing $Pd(NO_3)_2$ and 2,2′-bipy in the molar ratio of 1:2 did not show any activity towards FA decomposition over 1 h at 60 °C. It is thought that 2,2′-bipy is coordinated strongly to $Pd(NO_3)_2$, which might hinder the ligand exchange between nitrate and formate. When Na_2PdCl_4 was used, the corresponding absorbance peak could not be observed presumably due to the rapid reduction. The relatively slow decomposition rate with Pd complexes coordinated with chlorides may result from rapid aggregation following reduction, which is possibly induced by weakening zeta-potential of the initially formed Pd nanoparticles.[18]

Formate anion is known to reduce Pd^{2+} complexes such as $Pd(OAc)_2$ by ligand exchange between acetate and formate, and produce Pd^0 species along with the generation of CO_2 and H_2.[19,20] Recently, a Pd^{2+} complex was *in situ* reduced by FA or formate and the generated Pd^0 species exhibited high catalytic activity towards dehydrogenation of FA.[21] An alternative explanation for the observed experimental results is that the Pd^{2+} cation also acted as a homogeneous catalytic site for FA decomposition, thus releasing CO_2 and H_2. Subsequently, the generated H_2 could reduce Pd^{2+} ion into Pd^0 species, which could then participate in FA dehydrogenation reaction. Experimentally, Pd^{2+} complexes were reduced rapidly upon direct exposure to molecular hydrogen with a rate of 30 mL/min under the reaction conditions without FA or sodium formate addition. Nonetheless, it cannot be concluded which pathway is responsible for the experimental observation, and both reaction pathways are possible. However, in either case, the formation of Pd–H species via C–H bond activation of formate is one of the important processes for FA decomposition over Pd^{2+} cation. Accordingly, we followed plausible reaction pathways for FA decomposition using different Pd^{2+} complexes.

2.2. Possible Pathways for Formic Acid Decomposition over (X–CO_2)Pd(O_2C–H) (X=F, H, CH_3, and NH_2)

Previously, iridium(III)-based catalyst exhibited good activities for aqueous phase FA dehydrogenation, and possible pathways were also explored using DFT calculations in the gas phase.[22] We employed Pd complexes coordinated with formate and X–CO_2 (X=H, CH_3, NH_2 and F) anions to follow plausible pathways for FA dehydrogenation over Pd^{2+} ion. Diverse functionalities (X) with different electronic properties were introduced to generate four complexes, (**X**–CO_2)Pd(O_2C–H) (**1**, X=H; **2**, X=CH_3; **3**, X=NH_2; and **4**, X=F) (Scheme 1). Note that the coordinated formate ligand in **1**–**4** also acts as the reactant for FA decomposition.

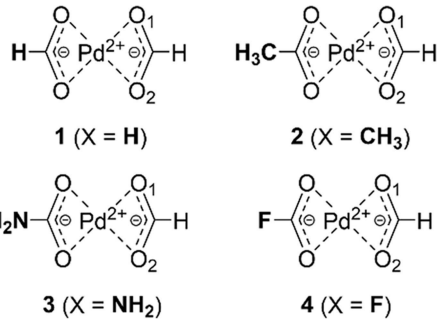

Scheme 1. (**X**–CO_2)Pd(O_2C–H) complexes.

The produced model complexes, **1**–**4** can result in C–H bond activation at formate anion via multiple steps, which could potentially release hydrogen from FA. For instance, **1** can be formed by the interaction between Pd^{2+} ion and formate, *i.e.*, FA gets dissociated into formate ion and proton (Eq. 3), and the formate anion ($HCOO^-$) coordinates to free Pd^{2+} cation to produce **1** (Eq. 4). The Pd complex can then change oxygen binding mode from η^2 to η^1 by rotating one of the coordinated formate ions (Eq. 5), followed by consecutive β-hydride elimination to yield (HCOO)Pd(H)(CO_2) (Eq. 6). Lastly, the formed Pd–H species reacts with FA, releasing molecular H_2 and CO_2 along with the regeneration of **1** (Eq. 7). The overall reaction is the desired FA dehydrogenation (Eq. 8). The FA decomposition pathway involving sequential steps of formate rotation and β-hydride elimination was consistent with those using Fe^{2+} system reported previously.[23–25]

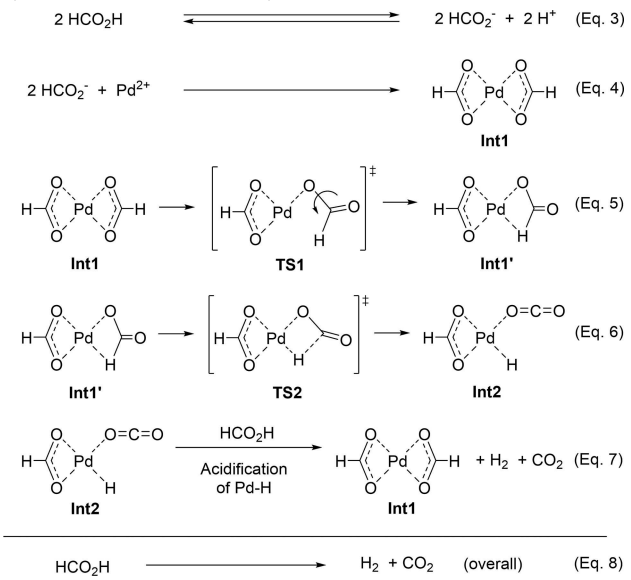

Based on the hypothetical dehydrogenation pathway, relevant geometries for each intermediate (Int) and transition state (TS) associated with **1**–**4** were optimized, and their energies were calculated in the gas phase (Figure 3a). The

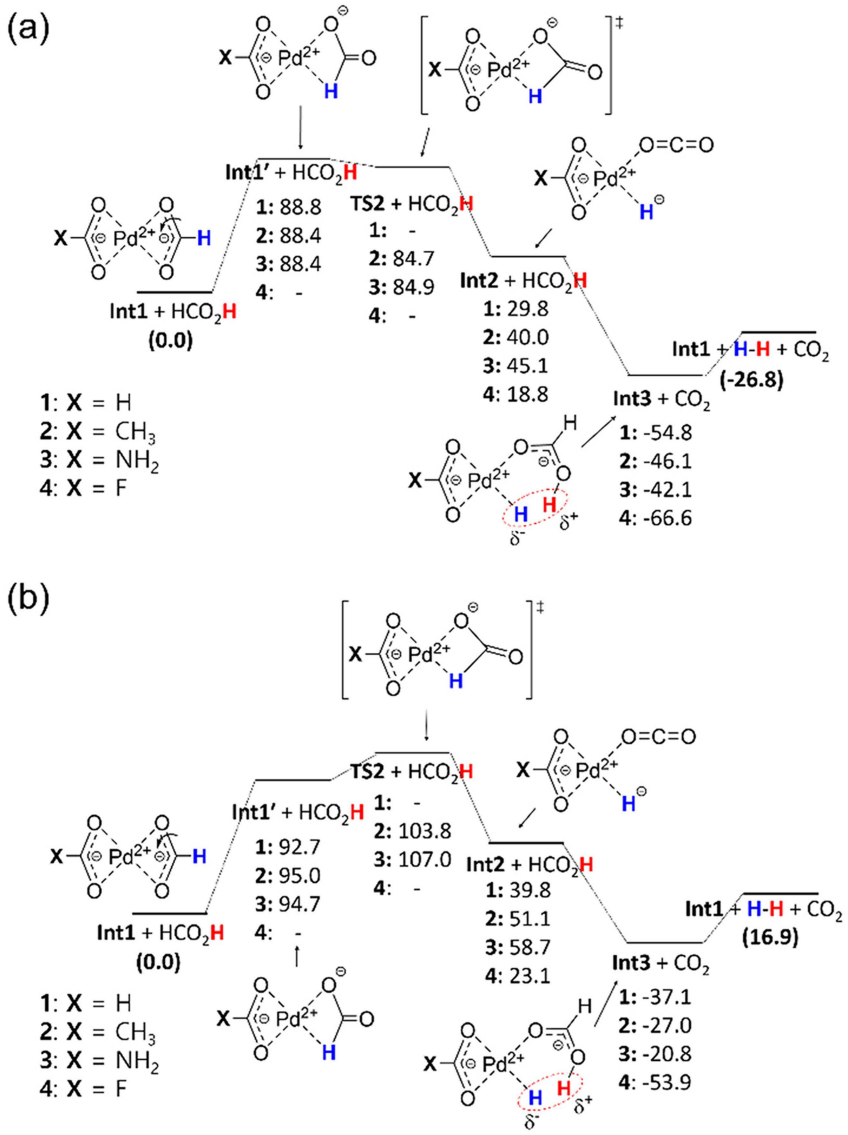

Figure 3. Calculated electronic energies (ΔE) of FA dehydrogenation over **1**–**4**: a) gas phase and b) solvent field (H_2O).

optimized Int and TS structures were further employed to compute additional electronic energies to simulate an aqueous phase FA dehydrogenation using conductor-like polarizable continuum model (CPCM) (Figure 3b). For details, **1**–**4** undergo an isomerization reaction possibly via TS1(Eq. 5) to produce **Int1′**, where oxygen and hydrogen atoms of a formate ligand interact simultaneously with the Pd^{2+} ion (Figure 3a). Compared to Pd–O1 and Pd–O2 (**1**, 2.106 Å; **2**, 2.113 Å; **3**, 2.116 Å) of **Int1**, the Pd–O1 bond lengths in **Int1′** shortened slightly to 2.060 Å, 2.074 Å, and 2.075 Å for **1**–**3**, respectively. Notably, the C–H bond length of the rotated formate ligand in **Int1′** was found to be 1.292 Å, 1.305 Å, and 1.291 Å for **1**–**3**, respectively, which indicated a significant elongation compared to those (**1**–**3**, 1.084 Å) of **Int1** (Table 1). In addition, the bond distances between Pd and H atoms in **Int1′** associated with **1**–**3** are 1.774 Å, 1.756 Å, and 1.769 Å, respectively. Moreover, the O1–C1–O2 bond angles are 140.4° (**Int1′-1**), 140.5° (**Int1′-2**), and 139.8° (**Int1′-3**), respectively, suggesting that the initial sp^2 hybridizations with the O1-C1-O2 angles of 116–117° at formate carbon of **Int1** were altered significantly. The results strongly imply that the C–H bond in each **Int1′** was activated partially either by changing the formate binding mode or by binding a free formate anion in this fashion. For **4**, **Int1′** structure could not be optimized successfully at the level of theory employed; instead, the initial structure was optimized directly to **Int2**, suggesting the complete C–H bond cleavage in the formate ligand. The result may originate from relatively electron deficient Pd^{2+} center of **4**, which is prone to have more electron density by hydride abstraction. The optimized structures of **Int1** and **Int1′** for **1**–**3** are illustrated in Figure S1 in the supplementary information. The relative electronic energies of **Int1′** with respect to **Int1** were calculated to be 88.8, 88.4, and 88.4 kJ mol^{-1} for **1**–**3**, respectively, in the gas phase (Figure 3a). However, these energies changed considerably upon single

Table 1. Selected Geometrical Parameters of **1**–**3**.

(H–COO)Pd(OOC–H) (**1**)						
	Pd–O1 [Å]	Pd–O2 [Å]	Pd–H1 [Å]	C–H1 [Å]	<O1–Pd–O2 [°]	<O1–C1–O2 [°]
Int1	2.105	2.106	–	1.084	63.2	116.6
Int1′	2.060	–	1.774	1.292	–	140.4
Int2	2.173	–	1.527	3.220	–	177.7
Int3	–	–	1.554	–	–	–
(CH_3–COO)Pd(OOC–H) (**2**)						
	Pd–O1 [Å]	Pd–O2 [Å]	Pd–H1 [Å]	C1–H [Å]	<O1–Pd–O2 [°]	<O1–C1–O2 [°]
Int1	2.113	2.113	–	1.084	63.0	116.9
Int1′	2.074	–	1.756	1.305	–	140.5
TS2	2.108	–	1.663	1.478	–	146.5
Int2	2.175	–	1.533	3.213	–	177.7
Int3	–	–	1.562	–	–	–
(NH_2–COO)Pd(OOC–H) (**3**)						
	Pd–O1 [Å]	Pd–O2 [Å]	Pd–H1 [Å]	C1–H [Å]	<O1–Pd–O2 [°]	<O1–C1–O2 [°]
Int1	2.116	2.116	–	1.084	63.0	117.0
Int1′	2.075	–	1.769	1.291	–	139.8
TS2	2.116	–	1.653	1.515	–	147.4
Int2	2.174	–	1.537	3.199	–	177.7
Int3	–	–	1.566	–	–	–
(F–COO)Pd(OOC–H) (**4**)						
	Pd–O1 [Å]	Pd–O2 [Å]	Pd–H1 [Å]	C1–H [Å]	<O1–Pd–O2 [°]	<O1–C1–O2 [°]
Int1	2.095	2.096	–	1.083	63.4	116.3
Int2	2.157	–	1.523	3.276	–	177.7
Int3	–	–	1.546	–	–	–

point energy computation with the conduct-like polarizable continuum model (CPCM) using the dielectric constant of water (Figure 3b). The relative energies for **Int1′** calculated with the CPCM model changed to 92.7 kJ mol^{-1} (**Int1′-1**), 95.0 kJ mol^{-1} (**Int1′-2**), and 94.7 kJ mol^{-1} (**Int1′-3**), which are higher than those obtained in the gas phase. These results may likely be due to the relative extent of stabilization of the optimized intermediate structures upon utilization of the CPCM model.

The transition state, **TS1** (see Eq. 5), which could be responsible for the rotational process from **Int1** to **Int1′** involves the cleavage of C=O bond with the bond order of 1.5, but no relevant TS structures for **1**–**4** could be obtained properly upon optimization without any geometrical constraints at the level of theory employed. Further optimization was carried out to locate potential transition states by freezing the coordination of atoms not involved in the formate rotation; *i.e.*, only oxygen and hydrogen atoms of the formate ion were fully relaxed upon optimization. The obtained optimized structures of **TS1** associated with **1**–**4** are shown in Figure S2. The electronic energies of **TS1** for **1**–**4** were computed to be 87.1 kJ mol^{-1} (**TS1-1**), 11.4 kJ mol^{-1} (**TS1-2**), 35.6 kJ mol^{-1} (**TS1-3**), 113.4 kJ mol^{-1} (**TS1-4**) in the gas phase. The results show that the relative **TS1** energies decreased significantly upon utilization of stronger electron donating ligands. When the CPCM model was employed, however, the relative energy differences became small. In addition, compared to those obtained in the gas phase, the transition state energies increased to 123.3 kJ mol^{-1} (**TS1-1**), 122.1 kJ mol^{-1} (**TS1-2**), 121.4 kJ mol^{-1} (**TS1-3**), and 125.5 kJ mol^{-1} (**TS1-4**). Given the relative **TS1** and **Int1′** energies, the **TS1** structures obtained with geometry constraints may not be the true transition state geometries. It should be noted that **TS1** is not necessary to follow FA dehydrogenation because formate can be bound directly to the Pd^{2+} center with a η^1-oxygen binding mode (**Int1′**) in the gas phase or a condensed (aqueous) phase. In other words, **Int1′** is the reactant for H_2-release from FA.

Next, **Int1′** undergoes β-hydride elimination, a hydrogen abstraction from C–H at the Pd^{2+} center via **TS2** to produce **Int2** where Pd–H species is present. The **TS2** structures for **2** and **3** were optimized successfully without any symmetry constraints (Figure S3). Important geometrical parameters are listed in Table 1. The calculated C–H bond lengths for **2** and **3** are 1.478 Å and 1.515 Å, respectively, which are 30% and 33% longer than that of free formate ion (1.136 Å). In addition, the Pd–H bond distances were computed to be 1.663 Å (**2**) and 1.653 Å (**3**). Moreover, O1–C1–O2 angles of the formate moieties in **2** and **3** were 146.5° and 147.4°, respectively. These results suggest that the initial sp^2 hybridization at the formate carbon was altered significantly, and the C–H bond in the formate species was cleaved considerably, along with the partial formation of the Pd–H bond in **TS2**. Intrinsic reaction coordination (IRC) calculations were performed using the obtained **TS2** structures, confirming the formation of **Int1′** and **Int2** through the reaction coordinates. Note that the calculated energies of **TS2** for **2** and **3** are 3.5–3.7 kJ mol^{-1} lower than those of **Int1′**, implying that potential energy surface near **Int1′** and **TS2** could be nearly flat. However, the corresponding **TS2** energies of **2** and **3** calculated using the CPCM model are 8.8 and 12.3 kJ mol^{-1} higher than those obtained in the gas phase.

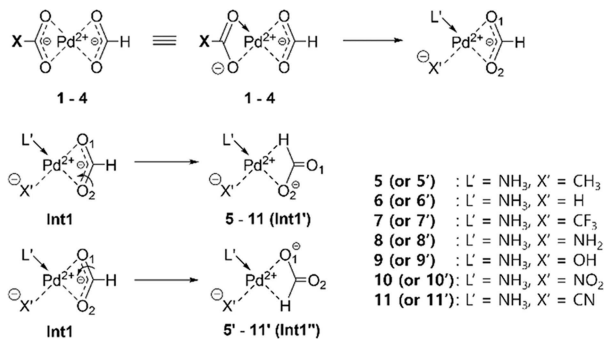

Figure 4. Additional Pd complexes coordinated with NH_3 as a neutral ligand and different anionic ligands (**5**–**11** and **5′**–**11′**).

To further scrutinize the nature of **TS2**, additional analyses were needed.

Int2 was then obtained from **Int1′** via **TS2**. In **Int2**, Pd–H species was produced by complete cleavage of the C–H bond of the formate ion along with the interaction of CO_2 with the Pd^{2+} center. The optimized structures for **Int2** are shown in Figure S4, and relevant geometrical parameters are listed in Table 1. The Pd–H bond lengths associated with **1**–**4** are 1.527 Å (**Int2-1**), 1.533 Å (**Int2-2**), 1.537 Å (**Int2-3**), and 1.523 Å (**Int2-4**), respectively, showing that a ligand with more electron donating ability resulted in an increased Pd–H bond length. Besides, the distance between carbon and hydrogen atoms in the formate anion increased drastically to >3.1 Å, clearly indicating the complete scission of the C–H bonds. Additionally, the O1–C–O2 angles in the optimized **Int2** are nearly 180°, indicating the sp-hybridization around the carbon atom with two oxygen atoms. The gas phase electronic energies of **Int2** are 29.8 kJ mol^{-1} (**Int2-1**), 40.0 kJ mol^{-1} (**Int2-2**), 45.1 kJ mol^{-1} (**Int2-3**), 18.8 kJ mol^{-1} (**Int2-4**), and were found to increase in the order of **3** > **2** > **1** > **4**. The trend appears to be correlated with the electronic properties of the ligands, and the **Int2** energy increases as a ligand provides more electron density to the Pd^{2+} ion. With the CPCM model, these gas phase energies again increased to 39.8 kJ mol^{-1} (**Int2-1**), 51.1 kJ mol^{-1} (Int2-**2**), 58.7 kJ mol^{-1} (Int2-**3**), 23.1 kJ mol^{-1} (**Int2-4**).

Finally, the formed **Int2** was interacted with FA to produce **Int3**, ultimately regenerating **Int1** along with the release of H_2. The optimized structures are depicted in Figure S5, and relevant bond lengths and angles are listed in Table 1. Mulliken charge analyses with **Int3** revealed that the negative charges of hydride attached to Pd increased as more electron donating ligands are coordinated: $\delta = -0.028$ (**Int3-1**), $\delta = -0.042$ (**Int3-2**), $\delta = -0.045$ (**Int3-3**), $\delta = -0.010$ (**Int3-4**). Consistent with the results, hydrogen atoms attached to FA had decreased positive charge as ligands with more electron donating functionalities were employed. Notably, dihydrogen bonding interactions between Pd-***H*** (δ^-) and HCOO-***H*** (δ^+) were found in the structures. Through the dihydrogen bonding interaction, molecular hydrogen can readily be released.[26] The calculated energy differences between **Int3** + CO_2 and **Int1** + HCOOH increased with the strength of electron donating ligand: −54.8 kJ mol^{-1} (**Int3-1**), −46.1 kJ mol^{-1} (**Int3-2**), −42.1 kJ mol^{-1} (**Int3-3**), −66.6 kJ mol^{-1} (**Int3-4**). In contrast to other processes, this step was found to be exothermic, partly because of the dihydrogen bonding interaction. As in the case of **Int2**, the CPCM method showed increased energies of −37.1 kJ mol^{-1} (**Int3-1**), −27.0 kJ mol^{-1} (**Int3-2**), −20.8 kJ mol^{-1} (**Int3-3**), −53.9 kJ mol^{-1} (**Int3-4**). The energy of the overall reaction, HCOOH→H_2 + CO_2 was calculated to be −26.8 kJ mol^{-1} in the gas phase and 16.9 kJ mol^{-1} with the CPCM model. The enthalpy and Gibbs free energy of FA dehydrogenation calculated in the gas phase are −19.6 kJ mol^{-1} and −49.8 kJ mol^{-1}, respectively, which are in good agreement with those obtained using NIST database.[27] The enthalpies and Gibbs free energies of the intermediates and transition states of **1**–**4** calculated at 298.15 K and 1 atm are listed in Table 2. The reaction pathways with enthalpies and Gibbs free energies (ΔG) involving **1**–**4** are illustrated in Figure S6.

2.3. Influence of Coordinated Ligands on FA Dehydrogenation over (X′)(L′)Pd(O_2C–H)

The model complexes, **1**–**4** possess the formate anion as a coordinating ligand with C=O bond order of 1.5. The two oxygen atoms in the formate anion can also be considered as a combination of a neutral (RC=O) and anionic (RC–O$^-$) ligands. In this context, we generated a number of different Pd complexes, (L′)(X′)Pd(O_2C–H) (**Int1**) where L′ and X′ represent a neutral ligand and an anionic ligand, respectively (Figure 4), and continued to investigate potential influence of the coordinating ligands on FA decomposition. In particular, we chose ammonia as a neutral ligand for L′ because amines are common neutral ligands that stabilize metal ions in numerous organometallic compounds. In contrast to **1**–**4**, **Int1** structures possessing distinct anionic ligands can follow two different pathways towards FA decomposition depending on the direction of formate rotation; *i.e.*, rotation of the H–C–O1 moiety at formate along C–O2 axis produces **5**–**11** while that of H1–C–O2 at formate along C–O1 axis gives **5′**–**11′**. Alternatively, the direction of formate coordination to Pd^{2+} ion, in conjunction with formate dissociation from a Pd^{2+} ion and consecutive coordination, could also affect the formation of either **Int1′** or **Int1″**, ultimately affording a different FA decomposition pathway. Since energetics for FA decomposition would vary depending on the kind of ligand attached to Pd^{2+}, relevant intermediates and transition states were optimized to elucidate key controlling factors for FA decomposition.

Figure 5 represents the gas phase FA dehydrogenation pathways over selected complexes coordinated with electron donating functionalities. Compared to **Int1**, the **Int1′-5** structure exhibits a lower energy of −29.2 kJ mol^{-1} while **Int1″-5′**, in which ammonia is located *trans* to hydride (H–Pd), shows a higher energy of 95.2 kJ mol^{-1}. Other complexes also display the similar trend. The calculated **TS2** energies with respect to **Int1** increase as X′ is more σ-donating ligands (**5**, –CH_3; **6**, –H) than π-donating ligands (**8**, –NH_2; **9**, –OH). The relative energies ($\Delta E_{TS2\text{-}Int1}$) for **5** and **6** are nearly identical, but the energy

Table 2. Electronic energies, enthalpies, and Gibbs free energies of intermediates and transition states for FA dehydrogenation over **1**–**4**, calculated at 298.15 K and 1 atm (Energies in Hartrees).

	E	H	G	E (water)[a]
H_2	−1.169505	−1.1662	−1.180995	−1.179726
CO_2	−188.638985	−188.635426	−188.660330	−188.653085
HCOOH	−189.798285	−189.794169	−189.822364	−189.839230
HCO_2^-	−189.256234	−189.252309	−189.280035	−189.380156
(H–COO)Pd(OOCH) (**1**)				
Int1	−506.193507	−506.185320	−506.226178	−506.258376
Int1′	−506.159702	−506.151168	−506.193238	−506.223061
Int2	−506.182145	−506.172693	−506.218335	−506.243233
Int3	−507.373672	−507.364215	−507.410479	−507.458638
TS1	−506.160349	−506.156039	−506.190074	−506.211403
(CH_3–COO)Pd(OOCH) (**2**)				
Int1	−545.497019	−545.487043	−545.532869	−545.589249
Int1′	−545.463360	−545.453054	−545.499970	−545.553082
Int2	−545.481768	−545.470549	−545.521679	−545.569772
Int3	−546.673861	−546.662676	−546.713429	−546.785695
TS1	−545.492684	−545.488376	−545.522883	−545.542756
TS2	−545.464764	−545.454628	−545.501246	−545.549695
(NH_2–COO)Pd(OOCH) (**3**)				
Int1	−561.564296	−561.554978	−561.598524	−561.650754
Int1′	−561.530642	−561.521015	−561.565646	−561.614694
Int2	−561.547124	−561.536576	−561.584920	−561.628415
Int3	−562.739614	−562.729122	−562.777030	−562.844826
TS1	−561.550718	−561.546411	−561.580909	−561.604525
TS2	−561.531945	−561.522430	−561.566885	−561.610014
(F–COO)Pd(OOCH) (**4**)				
Int1	−605.453473	−605.444520	−605.487676	−605.510275
Int2	−605.446317	−605.436069	−605.484170	−605.501493
Int3	−606.638138	−606.628770	−606.673062	−606.716952
TS1	−605.410288	−605.405975	−605.440532	−605.462463

[a] Calculated using the conduct-like polarizable continuum model (CPCM) with the dielectric constant of H_2O.

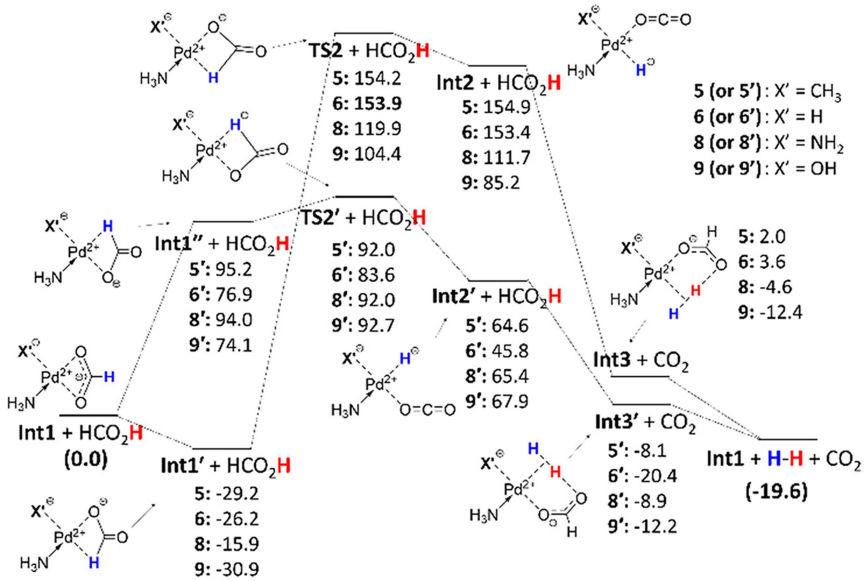

Figure 5. The electronic energies (ΔE) for FA dehydrogenation over complexes coordinated with electron donating ligands (**5**, **6**, **8**, **9** and **5′**, **6′**, **8′**, **9′**).

difference between **8** and **9** is 15.5 kJ mol^{-1}. For **TS2′**, the energy difference between **5′** and **6′** is 8.4 kJ mol^{-1} while that between **8′** and **9′** is negligible. Although **Int1″** is energetically higher than **Int1′**, the C–H bond activation processes via **TS2′** appears

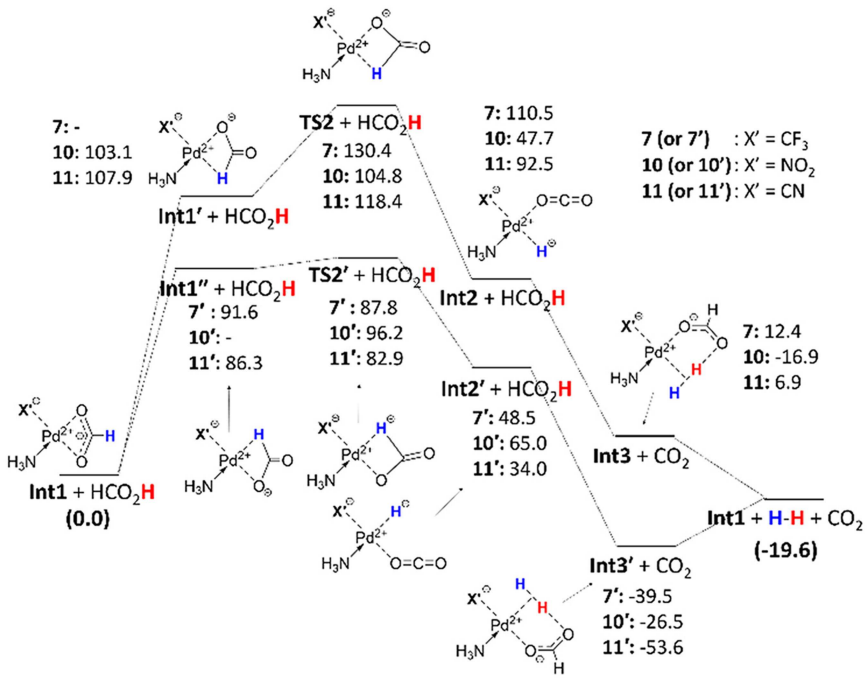

Figure 6. The electronic energies (ΔE) calculated in the gas phase for FA dehydrogenation over complexes coordinated with electron withdrawing ligands (**7**, **10**, **11** and **7′**, **10′**, **11′**).

to have no kinetic barrier or have small activation energies. In contrast, the corresponding step from **Int1′** to **Int2** via **TS2** was found to need a much higher energy (*e.g.*, $\Delta E_{TS2-Int1'}$ (**5**) = 183.4 kJ mol^{-1}). In the gas phase, the electronic energy of **TS2′-5′** is slightly lower compared to that of **Int1′′-5′** ($\Delta E_{TS2'-Int1''} = -3.2$ kJ mol^{-1}), which increases to $\Delta E_{TS2'-Int1''} = 20.4$ kJ mol^{-1} upon computation using the CPCM model with water. The difference in Gibbs free energies between **Int1′′** and **TS2′** at **5′** was calculated to be −3.3 kJ mol^{-1} (Figure S7). Similarly, **TS2′** associated with the complex **8′** showed slightly lower energy than the corresponding **Int1′′**, with $\Delta E_{TS2'-Int1''} = -2.0$ kJ mol^{-1} being achieved. In the cases of **6′** and **9′**, however, the differences in electronic energies between **Int1′′** and **TS2′** were found to increase significantly (**6′**, $\Delta E_{TS2'-Int1''} = 6.7$ kJ mol^{-1}; **9′**, $\Delta E_{TS2'-Int1''} = 18.6$ kJ mol^{-1}). As in the case of **1**–**4**, the negligible energy differences between **Int1′′** and **TS2′** for **5′** and **8′** again imply that the potential energy surface around the species could be nearly flat. These obtained results suggest that FA decomposition likely proceeds from **Int1** to **Int1′′** to produce **Int2′** via **TS2′**, which then reacts with an additional FA species to yield **Int3′** + CO_2. Finally, the **Int3′** structure produces molecular hydrogen (H_2) with the regeneration of **Int1**.

Other complexes coordinated with electron withdrawing ligands (**7**, **10**, **11**, and **7′**, **10′**, **11′**) were likewise found to undergo FA decomposition with the corresponding intermediates (**Int1′′** for **7′**, **10′**, and **11′**) involving the analogous transition states (**TS2′** for **7′**, **10′**, and **11′**) (Figure 6). The relevant reaction pathways involving **7**, **10**, **11**, and **7′**, **10′**, **11′** with Gibbs free energies are also depicted in Figure S8. Notably, at the **Int3′** structures shown in Figures 5 and 6, the H–H bond distances in **Int3′** that is coordinated with electron donating ligands (**5′**, 0.836 Å; **6′**, 0.847 Å; **8′**, 0.847 Å; **9′**, 0.846 Å) are much shorter than those (**1**, 1.678 Å; **2**, 1.630 Å; **3**, 1.603 Å; **4**, 1.741 Å) of **1**–**4** but slightly longer than that (0.744 Å) of free hydrogen. On the other hand, the H–H distances in **Int3′** that is attached to electron withdrawing ligands (**7′**, 1.546 Å; **10′**, 1.513 Å; **11′**, 1.587 Å) are much elongated. The results originate partly from relative electron density of the Pd^{2+} ion. Relatively more electron-deficient Pd^{2+} ions may tend to have hydride as a ligand in the coordinating spheres to afford increased H(δ^-)–H(δ^+) distances, whereas electron-rich Pd^{2+} ions can interact with molecular hydrogen-like species in a sigma (σ) fashion to allow strong interaction between H(δ^-) and H(δ^+).

Based on these pathways described above, the C–H bond dissociation (**TS2′**) and/or the formation of **Int1′′** is the rate determining step in the FA decomposition (Figures 5 and 6). The HOMO and LUMO structures of **TS2′** for **5′**–**11′** are summarized in Figure S9. We also examined the possibility of **TS1** (**Int1** to **Int1′**) or **TS1′** (**Int1** to **Int1′′**) as a potential rate controlling step by optimizing **TS1** and **TS1′** structures. Efforts towards optimization of relevant transition state structures for the formate rotation step were not successful. To obtain the desired structures, geometry optimization was carried out by freezing the coordination of atoms not involving the formate rotation. The calculated energies for **TS1′** are much lower than those of **Int1′′**. In case of **TS1**, most of the computed energies are higher than those of **Int1′**. The results strongly suggest that the **TS1** and **TS1′** structures optimized using geometry constraints may not be true transition states responsible for the isomerization between **Int1** and **Int1′** as well as between **Int1**

and **Int1**′′. In addition to **TS1**/**TS1**′, we further explored a transition state alternative to **TS2**/**TS2**′ involving interaction between formate hydrogen and Pd^{2+}, based on previous studies[28] where the hydrogen atom of the formate ligand was coordinated in a sigma (σ) fashion at one of the sites at a Pd^{2+} center possessing the square planar geometry. Upon repeated geometry optimization using **1** as a base complex, the targeted structure initially employed was optimized to yield **Int2** (see Figure 3a). The result likely comes from thermodynamically stable interaction between Pd^{2+} and η^2-OOCH using two sites of the square planar geometry; coordination of formate hydrogen in a η^1-fashion generates a vacant site around Pd^{2+}, which is thermodynamically unstable. The regenerated **Int1** species can re-enter the catalytic cycle or the produced hydrogen can further reduce Pd^{2+} at **Int1** to Pd^0. These reduced Pd^0 species can act as a new active site to accelerate FA decomposition continuously. The relative electronic energy for the Pd^{2+} reduction by H_2 was calculated to be $\Delta E = -240\ kJ\,mol^{-1}$ (**Int1** $+ H_2 \rightarrow Pd^0 + 2$ HCOOH). The high exothermicity of the Pd^{2+} reduction is consistent with the experimental observation.

Along with the pathways depicted in Figures 5 and 6, the Pd^{2+} reduction can also be facilitated by the produced Pd–H species, (L′)(X)Pd(H)(CO_2). As an example with **1**, (HCOO)Pd(H)(COO) (**Int2** in Figure 1a) can react with NH_3 in the gas phase to produce **6** (Eq. 9; $\Delta E = -286\ kJ\,mol^{-1}$). The isomerization of **Int1-6** again occurs to produce **Int1**′′**-6**′ (Eq. 10; $\Delta E = 74\ kJ\,mol^{-1}$), followed by β-hydride elimination to yield **Int2**′**-6**′ (Eq. 11; $\Delta E = -38\ kJ\,mol^{-1}$) via **TS2**′ ($\Delta E_{TS2'-Int1''} = 6.7\ kJ\,mol^{-1}$). The palladium dihydride, **Int2**′**-6**′ then proceeds reductive elimination to give the Pd^0 species (Eq. 12; $\Delta E = -158\ kJ\,mol^{-1}$). The overall ΔE for Eq. 13 is highly exothermic and computed to be $-408\ kJ\,mol^{-1}$, also supporting the Pd^{2+} reduction which was observed experimentally.

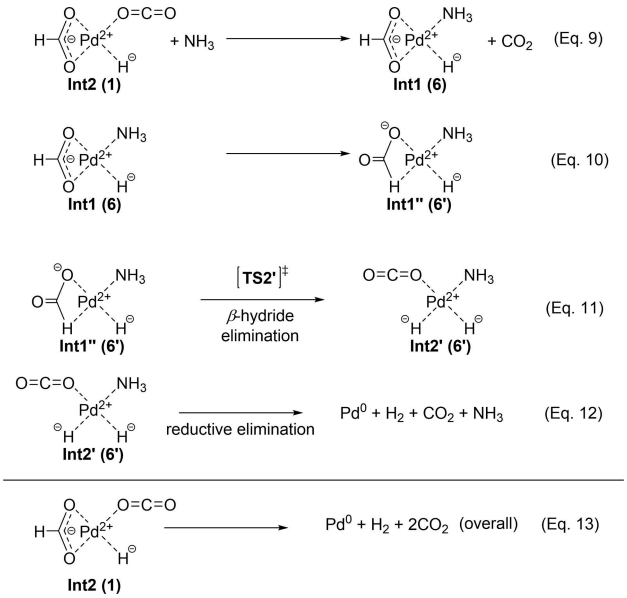

3. Conclusions

In summary, a series of aqueous Pd^{2+} complexes were tested in FA dehydrogenation reaction and examined computational pathways by DFT method. Experimental results indicate that $Pd(NO_3)_2$ was *in situ* reduced to metallic Pd^0 species during the course of the reaction and aqueous solution containing a Pd^{2+} precursor and mixtures of FA and SF generate effectively CO_2 and H_2 gas at 60 °C. Computational pathways were examined focusing on the Pd^{2+} state starting from Pd^{2+} with η^2-bound formate, β-hydride elimination, and subsequent CO_2 and H_2 elimination by formic acid. When (X–CO_2)Pd(O_2C–H) (X=F, H, CH_3, and NH_2) were examined, the formation of **Int1**′ and/or the C–H bond dissociation (**TS2**) is the rate determining step in the FA decomposition. In addition, electronic energies of β-hydride eliminated form (X–CO_2)Pd(H)(CO_2) (**Int2**) was found to be higher as X is more electron donating ligands. Influences of anionic coordinated ligands in FA dehydrogenation reaction with the formula (X′)(NH_3)Pd(O_2C–H) (X=CH_3, H, CF_3, NH_2, OH, NO_2, CN) were further explored. In all cases, rotation of formate where NH_3 trans to hydride ligand showed lower energy barriers than X trans to hydride ligand. Once η^2-bound formate with one oxygen and one hydrogen atoms interacts to Pd^{2+} center, scission of C–H bond proceeds with low activation barrier. Based on this study, further ligand design of Pd^{2+}-based catalysts is currently underway.

Experimental Section

General Information

Palladium(II) nitrate dihydrate ($Pd(NO_3)_2 \cdot 2H_2O$), palladium(II) chloride ($PdCl_2$), sodium tetrachloropalladate(II) (Na_2PdCl_4), tetrakis (acetonitrile)palladium(II) tetrafluoroborate ($Pd(CH_3CN)_4(BF_4)_2$), and palladium(II) actetate ($Pd(O_2CCH_3)_2$) were purchased from Sigma Aldrich. Tetraaminepalladium(II) chloride monohydrate ($Pd(NH_3)_4Cl_2 \cdot H_2O$), sodium formate ($HCO_2Na$), and 2,2′-bipyridine were purchased from Alfa Aesar. Unless otherwise noted, the compounds were used without further purification. UV-Vis spectra were measured on an Agilent Cary 100 UV-Vis spectrometer in the wavelength range from 300 to 800 nm, with a resolution of 1 nm. Standard quartz cuvettes with a 10-mm light path were used for all UV-Vis spectra measurements.

Dehydrogenation of Formic Acid/Formate over Pd(II) Complexes

In a typical reaction, a desired Pd^{2+} complex (94 μmol) was dissolved in distilled water (2.0 mL) in a glass tube, and purged by nitrogen and heated to 60 °C. An aqueous mixture (2.5 mL) of formic acid (9 mmol) and sodium formate (9 mmol) was then injected into the reactor and stirred vigorously. The volume of released gas was measured using an automatic gas burette system, which was directly connected to the reactor for real-time volumetric measurement. For in situ UV-Vis spectroscopic analyses with different Pd(II) complexes, an aqueous solution (1.2 mL) containing a desired Pd compound (0.29 μmol) was added into a cuvette. Then an additional aqueous solution (1.5 mL) containing formic acid (5.4 mmol) and sodium formate (5.4 mmol) was added

to it. The resulting mixture was monitored by UV-Vis spectroscopy at regular intervals of 5 min for 60 min.

Computational Details

Density functional theory (DFT) calculations with Pd species coordinated to different ligands were carried out using the Gaussian 09 package.[29] All ground states, transition states, and intermediate geometries along the reaction pathways were fully optimized in the gas state using the B3LYP functional[30] with 6-311 + +G(2d,p) basis set for carbon, nitrogen, oxygen, and fluorine atoms in conjunction with the SDD(MWB28) basis set[31] for Pd atom without any symmetry constraints except the rotational process (**TS1** or **TS1′**). The **TS1** geometries were optimized by freezing the coordinates of atoms not involved in the rotational process; *i.e.*, only the oxygen and hydrogen atoms of formate at both (X–CO_2)Pd(OC**OH**) (**1**–**4**) and (L)(X)Pd(OC**OH**) (**5**–**9**) were relaxed. Harmonic vibrational analyses were performed on the optimized geometries at the same level to establish the nature of stationary points as well as to compute zero point energies. All reported energies were corrected using the obtained zero point energies. All stationary points optimized had no imaginary vibrational frequency except (F-COO)Pd(H)(HCOOH) (**Int3** (**4**)), (CH_3)(NH_3)Pd(H)(HCOOH) (**Int3** (**5**)), (CN)(NH_3)Pd(OOCH) (**Int1** (**11**)), and (CF_3)(NH_3)Pd(H)(CO_2) (**Int2** (**7**)) where small negative frequencies of less than $-15\ cm^{-1}$ were found. True first-order saddle points (**TS2** and **TS2′**) had only one imaginary frequency. Intrinsic reaction coordinate (IRC) calculations were carried out in both the forward and reverse directions to confirm the reaction pathways from the located transition states. In addition to the energy calculation in the gas phase, a solvent (water) effect was further considered using the conductor-like polarizable continuum model (CPCM)[32] with the geometries optimized in the gas phase. The calculated electronic energies, enthalpies, and Gibbs free energies at 298.15 K and 1 atm for all reactions at the level of theory are summarized in Tables 2, S2 and S4.

Acknowledgements

This work was supported by the Technology Development Program to Solve Climate Changes of the National Research Foundation (NRF) funded by the Ministry of Science, ICT & Future Planning (2015M1A2A2074688) as well as by the KIST institutional program funded by the Korea Institute of Science and Technology (2E28272).

Conflict of Interest

The authors declare no conflict of interest.

Keywords: decomposition pathway · density functional theory · formic acid · hydrogen storage · palladium

[1] P. Moriarty, D. Honnery, *Renewable Sustainable Energy Rev.* **2012**, *16*, 244–252.
[2] S. Singh, S. Jain, V. Ps, A. K. Tiwari, M. R. Nouni, J. K. Pandey, S. Goel, *Renewable Sustainable Energy Rev.* **2015**, *51*, 623–633.
[3] K. Mazloomi, C. Gomes, *Renewable Sustainable Energy Rev.* **2012**, *16*, 3024–3033.
[4] K. Sordakis, C. Tang, L. K. Vogt, H. Junge, P. J. Dyson, M. Beller, G. Laurenczy, *Chem. Rev.* **2018**, *118*, 372–433.
[5] D. L. Trimm, *Appl. Catal. A* **2005**, *296*, 1–11.
[6] C. Fellay, P. J. Dyson, G. Laurenczy, *Angew. Chem. Int. Ed.* **2008**, *47*, 3966–3968; *Angew. Chem.* **2008**, *120*, 4030–4032.
[7] C. Fellay, N. Yan, P. J. Dyson, G. Laurenczy, *Chem. Eur. J.* **2009**, *15*, 3752–3760.
[8] Y. Himeda, *Green Chem.* **2009**, *11*, 2018.
[9] S. Fukuzumi, T. Kobayashi, T. Suenobu, *ChemSusChem* **2008**, *1*, 827–834.
[10] A. Boddien, D. Mellmann, F. Gärtner, R. Jackstell, H. Junge, P. J. Dyson, G. Laurenczy, R. Ludwig, M. Beller, *Science* **2011**, *333*, 1733–1737.
[11] E. A. Bielinski, P. O. Lagaditis, Y. Zhang, B. Q. Mercado, C. Würtele, W. H. Bernskoetter, N. Hazari, S. Schneider, *J. Am. Chem. Soc.* **2014**, *136*, 10234–10237.
[12] Zhong, M. Iguchi, M. Chatterjee, Y. Himeda, Q. Xu, H. Kawanami, *Adv. Sustainable Syst.* **2018**, *2*, 1700161.
[13] J. H. Lee, J. Cho, M. Jeon, M. Ridwan, H. S. Park, S. H. Choi, S. W. Nam, J. Han, T.-H. Lim, H. C. Ham, C. W. Yoon, *J. Mater. Chem. A* **2016**, *4*, 14141–14147.
[14] W. Y. Yu, G. M. Mullen, D. W. Flaherty, C. B. Mullins, *J. Am. Chem. Soc.* **2014**, *136*, 11070–11078.
[15] Y. Ping, J.-M. Yan, Z.-L. Wang, H.-L. Wang, Q. Jiang, *J. Mater. Chem. A* **2013**, *1*, 12188.
[16] X. Wang, G.-W. Qi, C.-H. Tan, Y.-P. Li, J. Guo, J. X.-J. Pang, S.-Y. Zhang, *Int. J. Hydrogen Energy* **2014**, *39*, 837–843.
[17] D. A. Bulushev, M. Zacharska, E. V. Shlyakho, A. L. Chuvilin, Y. Guo, S. Beloshapkin, A. V. Okotrub, L. G. Bulusheva, *ACS Catal.* **2016**, *6*, 681–691.
[18] L. Zhao, D. Jiang, Y. Cai, X. Ji, R. Xie, W. Yang, *Nanoscale* **2012**, *4*, 5071–5076.
[19] B. Basu, S. Das, P. Das, A. K. Nanda, *Tetrahedron Lett.* **2005**, *46*, 8591–8593.
[20] S. V. Ley, C. Mitchell, D. Pears, C. Ramarao, J. Q. Yu, W. Zhou, *Org. Lett.* **2003**, *5*, 4665–4668.
[21] Q. L. Zhu, F. Z. Song, Q. J. Wang, N. Tsumori, Y. Himeda, T. Autrey, Q. Xu, *J. Mater. Chem. A* **2018**, *6*, 5544–5549.
[22] R. Tanaka, M. Yamashita, L. W. Chung, K. Morokuma, K. Nozaki, *Organometallics* **2011**, *30*, 6742–6750.
[23] F. Bertini, I. Mellone, A. Ienco, M. Peruzzini, L. Gonsalvi, *ACS Catal.* **2015**, *5*, 1254–1265.
[24] X. Yang, *Dalton Trans.* **2013**, *42*, 11987–11991.
[25] R. Sánchez-De-Armas, L. Xue, M. S. G. Ahlquist, *Chem. Eur. J.* **2013**, *19*, 11869–11873.
[26] R. H. Crabtree, *Chem. Rev.* **2016**, *116*, 8750–8769.
[27] NIST Chemistry WebBook, NIST Standard Reference Database Number 69, https://webbook.nist.gov/chemistry/ (accessed Nov 25, 2018).
[28] H. Ge, Y. Jing, X. Yang, *Inorg. Chem.* **2016**, *55*, 12179–12184.
[29] M. J. Frisch, G. W. Trucks, H. B. Schlegel, G. E. Scuseria, M. A. Robb, J. R. Cheeseman, G. Scalmani, V. Barone, G. A. Petersson, H. Nakatsuji, X. Li, M. Caricato, A. Marenich, J. Bloino, B. G. Janesko, R. Gomperts, B. Mennucci, H. P. Hratchian, J. V. Ortiz, A. F. Izmaylov, J. L. Sonnenberg, D. Williams-Young, F. Ding, F. Lipparini, F. Egidi, J. Goings, B. Peng, A. Petrone, T. Henderson, D. Ranasinghe, V. G. Zakrzewski, J. Gao, N. Rega, G. Zheng, W. Liang, M. Hada, M. Ehara, K. Toyota, R. Fukuda, J. Hasegawa, M. Ishida, T. Nakajima, Y. Honda, O. Kitao, H. Nakai, T. Vreven, K. Throssell, J. A. Montgomery, Jr., J. E. Peralta, F. Ogliaro, M. Bearpark, J. J. Heyd, E. Brothers, K. N. Kudin, V. N. Staroverov, T. Keith, R. Kobayashi, J. Normand, K. Raghavachari, A. Rendell, J. C. Burant, S. S. Iyengar, J. Tomasi, M. Cossi, J. M. Millam, M. Klene, C. Adamo, R. Cammi, J. W. Ochterski, R. L. Martin, K. Morokuma, O. Farkas, J. B. Foresman, D. J. Fox, *Gaussian 09*, revision A.02; Gaussian, Inc., Wallingford, CT, **2016**.
[30] A. D. Beke, *J. Chem. Phys.* **1993**, *98*, 5648–5652.
[31] D. Andrae, U. Haeussermann, M. Dolg, H. Stoll, H. Preuss, *Theor. Chem. Acc.* **1990**, *77*, 123–141.
[32] M. Cossi, N. Rega, G. Scalmani, V. Barone, D. Chimica, F. Ii, C. M. S. Angelo, *J. Comput. Chem.* **2003**, *24*, 669–681.

Manuscript received: November 26, 2018
Revised manuscript received: December 31, 2018
Version of record online: February 1, 2019